Electronic Supplementary Material (ESI) for Physical Chemistry Chemical Physics.

Supplementary information

Half-Raspberry-Like Bimetallic Nanoassembly: Interstitials Dependent Correlated Surface Plasmon Resonances and Surface-Enhanced Raman Spectroscopy

Mohammad Kamal Hossain[1, *] Yasutaka Kitahama[2] and Yukihiro Ozaki[2]

[1]*Interdisciplinary Research Center for Renewable Energy and Power Systems (IRC-REPS), Research Institute, King Fahd University of Petroleum & Minerals (KFUPM), Dhahran 31261, Kingdom of Saudi Arabia.*

[2]*School of Biological and Environmental Sciences, Kwansei Gakuin University, Gakuen 2-1, Sanda, Hyogo 669-1337, Japan.*

Correspondence to: kamalhossain@kfupm.edu.sa

1. Experimental setup for correlated measurements

Localized surface plasmon resonances (LSPRs) and subsequent plasmon-enhanced phenomena such as surface-enhanced Raman scattering (SERS) are sensitive to underlying specimen, particularly fine structure in nanoscale. Therefore, it is incumbent to carry out correlated SPR and SERS measurements at the very same position without any change of the target spot. A multifunctional and lab-built facility as shown below in Fig. SI1 was available in our disposal carry out such experiments in this regard.

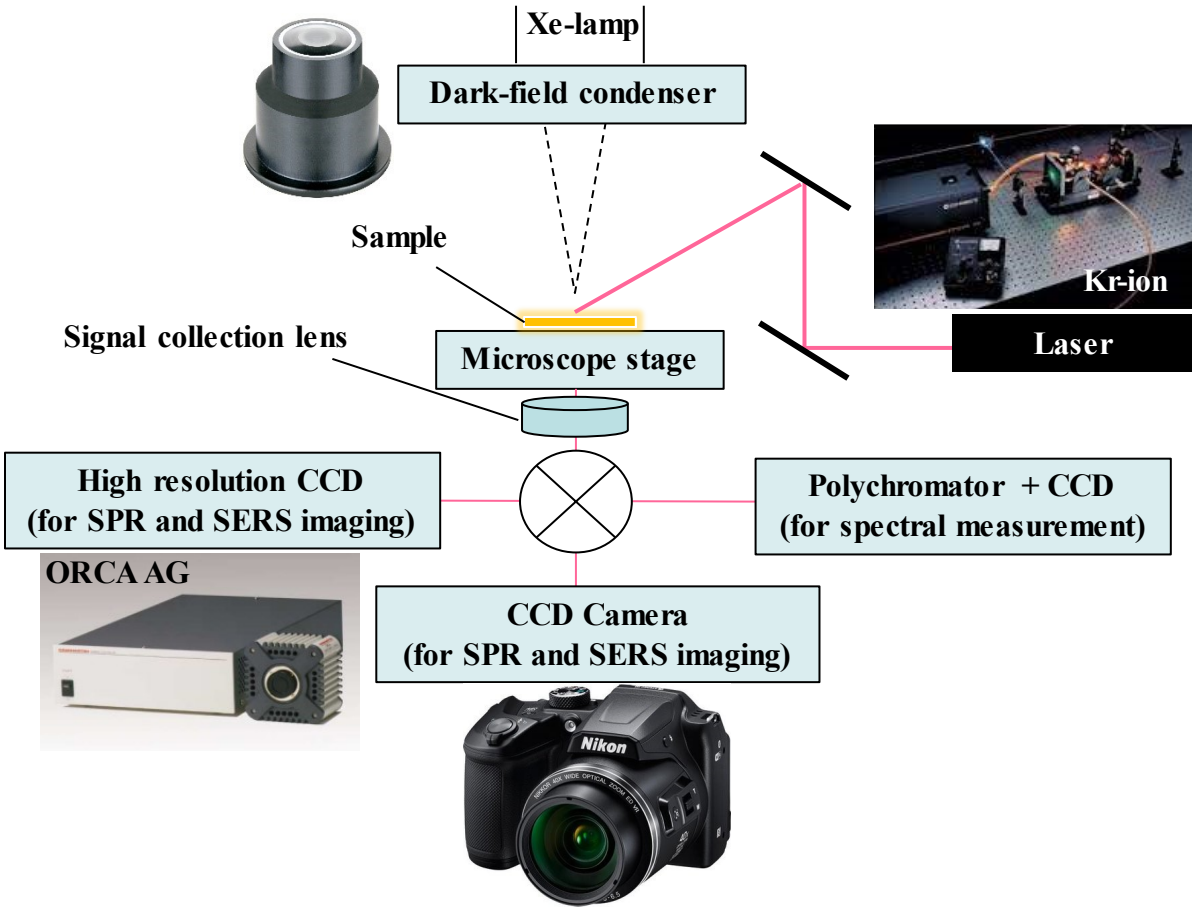

Figure SI1. A schematic diagram showing the multi-functional experimental setup for correlated spectroscopy combining dark-field microscopy and surface-enhanced Raman spectroscopy at the

very same spatially-resolved target spot along with high resolution CCD for SRP and SERS imaging and spectroscopy.

2. Extinction cross-section for Au tetramer with and without Ag mists:

Typical Au tetramer models with and without Ag mists as explained in the experimental section of main texts were analyzed by FDTD to calculate extinction cross-section. Fig. SI1a-c display such cross-section of the above-mentioned models excited at s-, p- and 45° of incident polarizations respectively. At s- and 45° of incident polarizations, Au tetramer with Ag mists showed plasmon peak at 515 nm with an additional peak located at 786 nm as shown in Fig. SI1a and Fig. SI1c. In

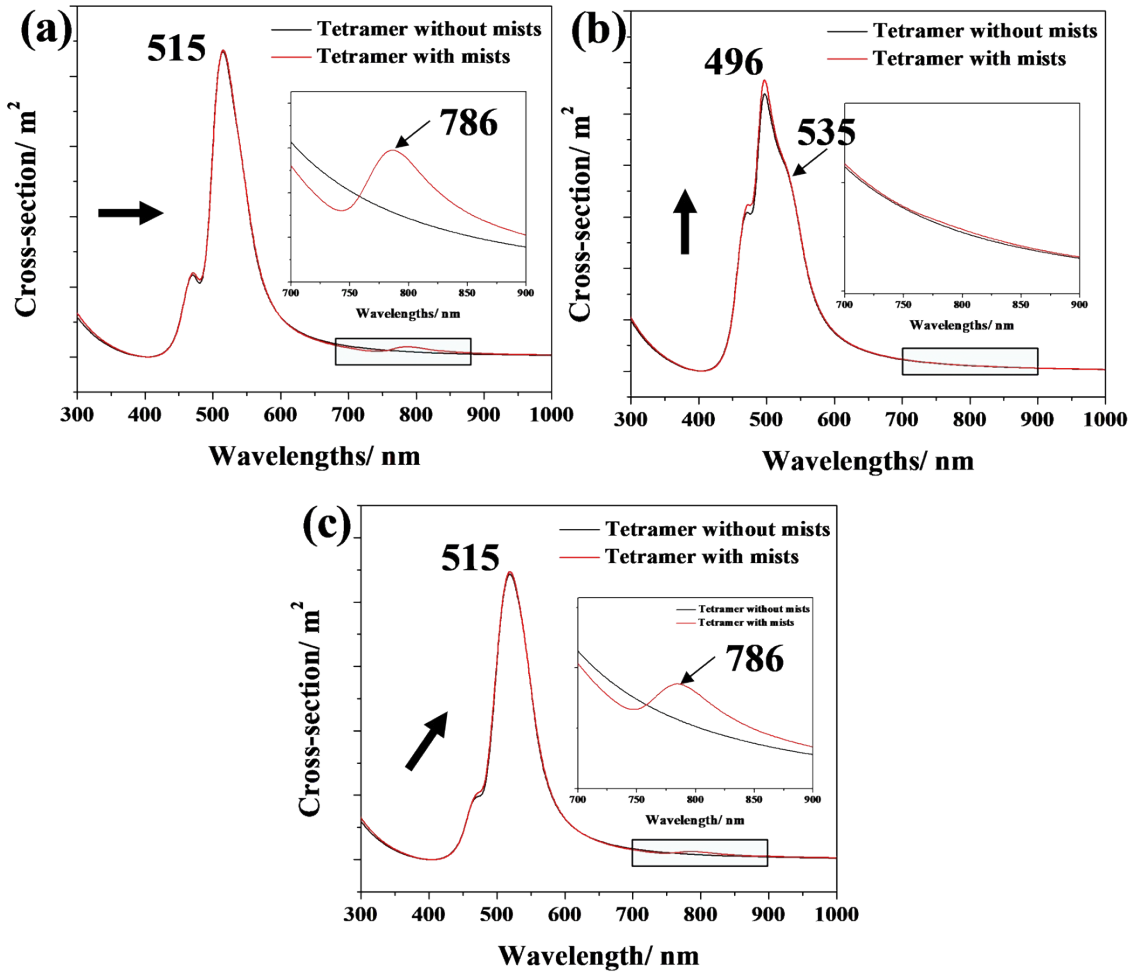

Figure SI2. (a)-(c) Simulated cross-section of the Au tetramer model with and without Ag mists at s-, p- and 45^o of incident polarizations respectively. The black arrow indicates the polarization direction.

case of p-polarization, a blue-shifted plasmon peak was observed in addition to a shoulder peak at 535 nm in both scenarios as shown in Fig. SI1b. This sort of modulation in plasmon peaks was supposed to influence the SERS enhancement as observed under this investigation.

3. EM near-field distributions at individual interstitials:

A tetramer unit of Au nanoparticles and the same model decorated with Ag mists were investigated by FDTD and corresponding EM near-field distributions at s-, p- and 45^o of incident polarizations were extracted. The tetramer under the simulation was having 2 interstitials along 2 horizontal axes (marked by 2 and 5), 2 interstitials along 2 interparticle axes of 45^o (marked by 1 and 4), and 1 interstitial along interparticle axes of 135^o (marked by 3). Four Ag mists were included in the modeling at Z=15 nm, placing three mists near the interstitials 1, 2, and 5 each, and one mist near the interstitials 3 and 4.

3.1 Au tetramer with and without Ag mists at s-polarization of incident excitation:

Figure SI2a represents EM near-field distributions along XY (Z= 0 nm) plane simulated at s-polarization. The inset at the left-top corner shows the model geometry that was used in the simulation. Two distinct interstitials marked as 2 and 5 and located along horizontal axes were found to possess the strongest EM near-field distribution of maximum intensity, E_{max}=13.64 V/m. Figure SI2b represents EM near-field distributions along XY (Z= 15 nm) plane simulated at s-polarization. In such a case, two distinct interstitials at the junction of Au and Ag near interstitials

2 and 5 and parallel to horizontal axes were found to possess the strongest EM near-field distribution of maximum intensity, E_{max}=14.42 V/m. Further detailed interstitials-wise EM near-

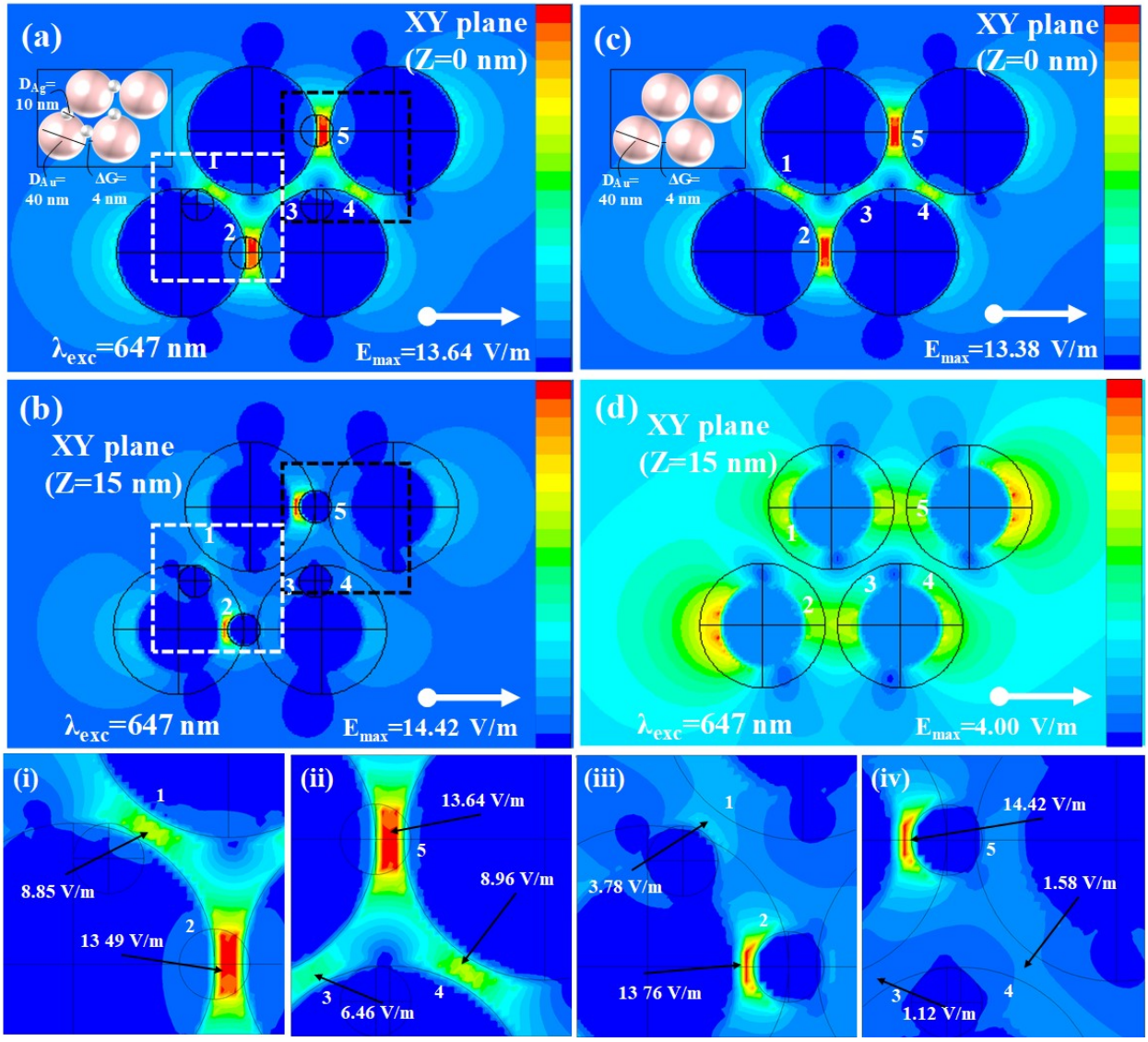

Figure SI3. (a) EM near-field distributions at XY (Z= 0 nm) plane of a typical model used in FDTD simulation for excitation of 647 nm at s-polarizations; inset: Model geometry of tetramer showing constituent Au nanoparticles (D_{Au}=40 nm) with 4 nm of interparticle gaps and decorated by Ag nanoparticles (D_{Ag}=10 nm). (b) EM near-field distribution at XY (Z= 15 nm) plane of the same model. (c)-(d) EM near-field distribution at XY (Z= 0 nm) and XY (Z= 15 nm) planes of the same model without Ag nanoparticles; inset: Model geometry of tetramer showing constituent Au nanoparticles (D_{Au}=40 nm) with 4 nm of interparticle gaps. Inset (i)-(ii): Magnified portions of EM near-field distributions as marked by white dashed square and black dashed square in Fig. SI2a respectively and inset (iii)-(iv): Magnified portions of EM near-field distributions as marked by white dashed square and black dashed square in Fig. SI2b

respectively. White arrows in each figure represent polarization directions of incident excitation. Colour bars represent the respective intensities observed under the simulations.

field distributions are elaborated in the latter part of the text. As for reference, the same model without the Ag mists was simulated and EM near-field distributions were extracted as shown in Fig. SI2c-d. Figure SI2c represents EM near-field distributions of such model along XY (Z= 0 nm) plane simulated at s-polarization. The inset at the left-top corner shows the model geometry that was used in the simulation. The interstitials marked as 2 and 5 and located along horizontal axes were found to possess the strongest EM near-field distributions of maximum intensity, E_{max}=13.38 V/m. Figure SI2d represents EM near-field distributions of the same model along XY (Z= 15 nm) plane simulated at s-polarization. With reference to those observed in Fig. SI2b, the EM near-field distributions were found weak (E_{max}=4.00 V/m). Further insight for individual interstitials is demonstrated in insets (i)-(iv). Inset (i)-(ii) represent magnified view of the EM near-field distributions as marked by white dashed and black dashed squared in Fig. SI2a respectively. It was noted that the strongest EM near-field distribution (E_{max}= 13.94 V/m) was confined to interstitial 2 associated with the one next to the strongest one at interstitial 1 (E_{max}=8.85 V/m) as shown in inset (i). Strongest EM near-field confinement at interstitial 2 was obvious because the incident polarization being parallel to the interparticle axis was favorable to the constructive dipole interaction at the interstitial marked by 2. Similarly, the strongest EM near-field distribution was found confined at interstitial 5 as shown in inset (ii). It was noteworthy that the interstitials 1, 3, and 4 were having reasonably high EM near-field distributions of E_{max}=8.85. 6.46 and 8.96 V/m respectively, although these interstitials were out of in-plane axes in such scenarios. Inset (iii)-(iv) represent magnified view of the EM near-field distributions as marked by white dashed and black dashed squared in Fig. SI2b respectively. The strongest EM near-field distribution, E_{max}= 13.76

V/m was found confined at the junction of Au nanoparticles and Ag mist located near the interstitial 2, whereas the EM near-field distribution at the junction of Au nanoparticle and Ag mist located near the interstitial 1 was found weak (E_{max}=3.78 V/m) as shown in inset (iii). Inset (iv) represents the EM near-field distributions covering interstitials 3, 4, and 5. Strongest EM near-field confinement (E_{max}=13.64 V/m) was observed at the junction of Au nanoparticle and Ag mist located near the interstitial 5 as shown in inset (iv). With reference to those observed in inset (ii), the junctions of Au nanoparticle and Ag mist near the interstitials marked as 3 and 4 as shown in inset (iv) were found very weak with EM near-field distribution of E_{max}= 1.12 and 1.58 V/m respectively. It was evident that in presence of Ag mists, the Au nanoassembly showed inhomogeneous EM near-field distributions as shown in insets (iii) and (iv). Such inhomogeneous EM near-field distributions were speculated to broaden the SPRs as was observed under this investigation and demonstrated in Fig. 4b in main texts. As a consequence of broadened and weak SPR, the corresponding SERS enhancements were supposed to have deteriorated. The very same phenomenon was observed in SERS measurements and demonstrated in Fig. 5c in main texts.

3.2 Au tetramer with and without Ag mists at p-polarization of incident excitation:

EM near-field distribution is known to be a function of incident polarization. Therefore, the same model was simulated by FDTD at p-polarization. At p-polarization, it was expected that any interstitial along the vertical axis would bear the strongest EM near-field distribution. However, since there were no interstitials along the vertical axis, interstitials along diagonal axes (e.g. 45^o and 135^o) were supposed to have appeared next to the strongest EM near-fields distribution. Indeed, confined EM-field distributions were observed at the interstitials along diagonal axes as shown in Fig. SI3. Figure SI3a represents EM near-field distributions along XY (Z= 0 nm) plane

simulated at p-polarization. Three interstitials marked as 1, 3, and 4 were found to possess the strongest EM near-field distribution of maximum intensity, E_{max}=11.24 V/m. Figure SI3b

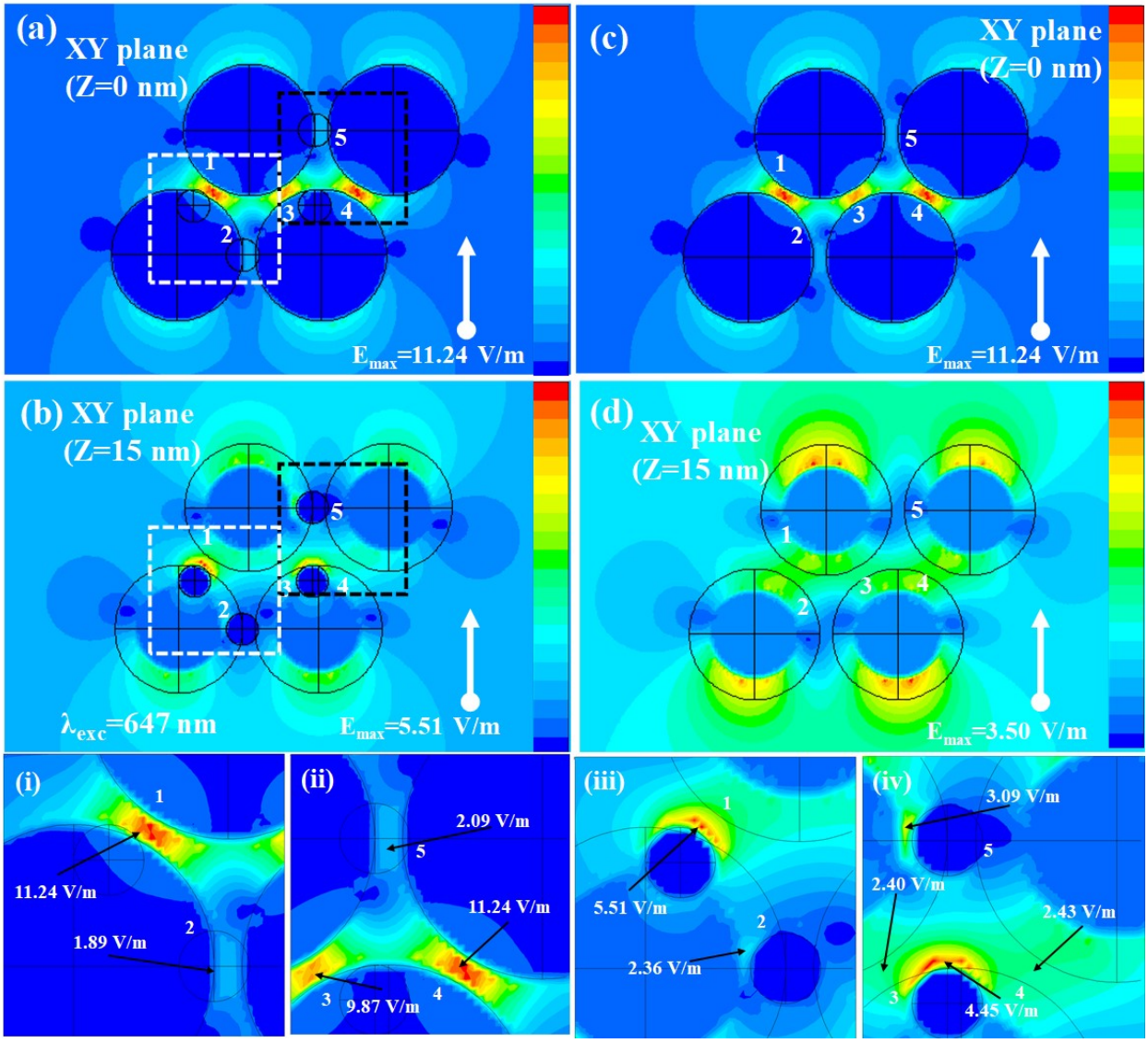

Figure SI4. (a) EM near-field distributions at XY (Z= 0 nm) plane of the same model as shown in the inset of Fig. SI2a and simulated for excitation of 647 nm at p-polarizations. (b) EM near-field distribution at XY (Z= 15 nm) plane of the same model. (c)-(d) EM near-field distribution at XY (Z= 0 nm) and XY (Z= 15 nm) planes of the same model without Ag nanoparticles as shown in the inset of Fig. SI2c. Inset (i)-(ii): Magnified portions of EM near-field distributions as marked by white dashed square and black dashed square in Fig. SI3a respectively and Inset (iii)-(iv): Magnified portions of EM near-field distributions as marked by white dashed square and black dashed square in Fig. SI3b respectively. White arrows in each figure represent polarization directions of incident excitation. Colour bars represent the respective intensities observed under the simulations.

represents EM near-field distributions along XY (Z= 15 nm) plane simulated at p-polarization. In such a case, two distinct interstitials at the junction of Au and Ag located near interstitials 1 and 3 and normal to horizontal axes were found to possess the strongest EM near-field distribution of maximum intensity, E_{max}=5.51 V/m. As for reference, the same model without the Ag mists was simulated and EM near-field distributions were extracted as shown in Fig. SI3c-d. Figure SI3c represents EM near-field distributions of such model along XY (Z= 0 nm) plane simulated at p-polarization. The interstitials marked as 1, 3, and 4 located along diagonal axes (e.g. 45^o and 135^o) were found to possess the strongest EM near-field distributions of maximum intensity, E_{max}=11.24 V/m. Figure SI3d represents EM near-field distributions of the same model along XY (Z= 15 nm) plane simulated at p-polarization. With reference to those observed in Fig. SI3b, the EM near-field distributions were found weak (E_{max}=3.50 V/m). Further insight for individual interstitials is demonstrated in insets (i)-(iv). Inset (i)-(ii) represent magnified view of the EM near-field distributions as marked by white dashed and black dashed squared in Fig. SI3a respectively. It was noted that the strongest EM near-field distribution (E_{max}= 11.24 V/m) was confined to interstitial 1 associated with a weak EM near-field distribution at interstitial 2 (E_{max}=1.89 V/m) as shown in inset (i). The strongest EM near-field confinement at interstitial 1 was obvious because the incident polarization being parallel to the vertical axis was partially favorable to the constructive dipole interaction at the interstitial marked by 1. Similarly, fairly strong EM near-field distributions were found confined at interstitial 3 and 4 (E_{max}=9.87 and 11.24 V/m) along with a weak EM near-field distribution of E_{max}= 2.09 V/m at interstitial 5 as shown in inset (ii). It was noteworthy that the interstitials 1, 3, and 4 were having reasonably high EM near-field distributions of E_{max}=11.24, 9.87, and 11.24 V/m respectively, although these interstitials were out of in-plane axes in such

scenarios. Inset (iii)-(iv) represent magnified view of the EM near-field distributions as marked by white dashed and black dashed squared in Fig. SI3b respectively. The strongest EM near-field distribution, E_{max}= 5.51 V/m was found confined at the junction of Au nanoparticles and Ag mist located near the interstitial 1, whereas the EM near-field distribution at the junction of Au nanoparticle and Ag mist located near the interstitial 2 was found weak (E_{max}=2.36 V/m) as shown in inset (iii). Inset (iv) represents the EM near-field distributions covering interstitials 3, 4, and 5. The strongest EM near-field confinement (E_{max}=4.45 V/m) was observed at the junction of Au nanoparticle and Ag mist located near the interstitial 3 as shown in inset (iv). The junction of Au nanoparticle and Ag mist located near the interstitial 5 was having reasonable high EM near-field distribution of E_{max}= 3.09 V/m. With reference to those observed in inset (ii), the junctions of Au nanoparticle and Ag mist near the interstitials marked as 3 and 4 as shown in inset (iv) were found very weak with EM near-field distribution of Emax= 2.40 and 2.43 V/m respectively.

3.3 Au tetramer with and without Ag mists at 45^o of incident polarization:

In the case of oblique incident polarization, two of the interstitials of tetramer being parallel to incident polarization under investigation were supposed to bear the strongest EM near-field distributions. Indeed, as shown in Fig. SI4a, two interstitials as marked by 1 and 4 were found confined with EM near-field distribution of Emax= 14.28 V/m. Figure SI4a represents EM near-field distributions along XY (Z= 0 nm) plane simulated at 45^o of incident polarization. Figure SI4b represents EM near-field distributions along XY (Z= 15 nm) plane simulated at 45^o of incident polarization. In such a case, two distinct interstitials at the junction of Au and Ag located near interstitials 2 and 5 were found to possess the strongest EM near-field distribution of maximum

intensity, E_{max}= 12.26 V/m. As for reference, the same model without the Ag mists was simulated

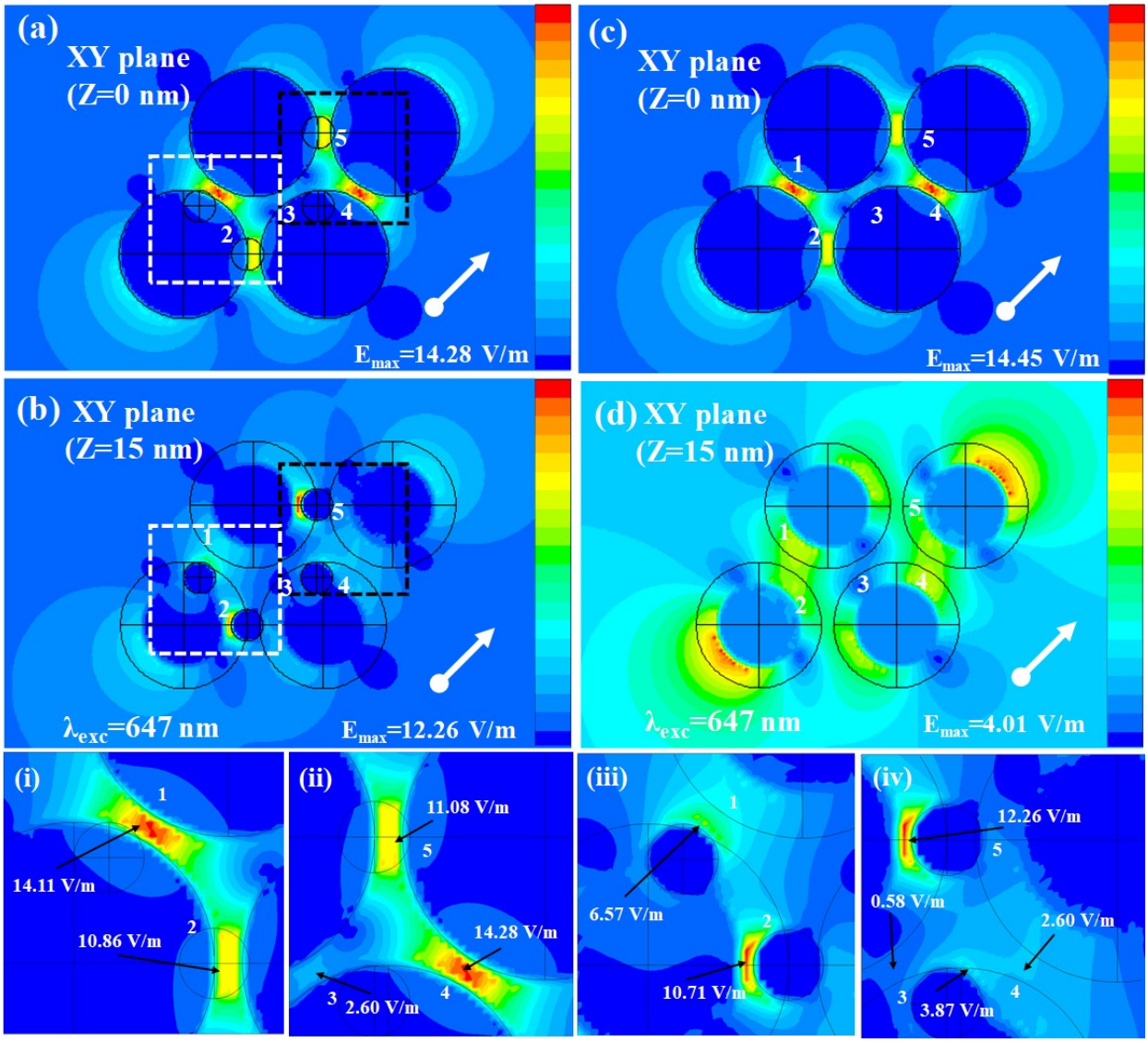

Figure SI5. (a) EM near-field distributions at XY (Z= 0 nm) plane of the same model as shown in the inset of Fig. SI2a and simulated for excitation of 647 nm at 45° of incident polarizations. (b) EM near-field distribution at XY (Z= 15 nm) plane of the same model. (c)-(d) EM near-field distribution at XY (Z= 0 nm) and XY (Z= 15 nm) planes of the same model without Ag nanoparticles as shown in the inset of Fig. SI2c. Inset (i)-(ii): Magnified portions of EM near-field distributions as marked by white dashed square and black dashed square in Fig. SI4a respectively and Inset (iii)-(iv): Magnified portions of EM near-field distributions as marked by white dashed square and black dashed square in Fig. SI4b respectively. White arrows in each figure represent polarization directions of incident excitation. Colour bars represent the respective intensities observed under the simulations.

and EM near-field distributions were extracted as shown in Fig. SI4c-d. Figure SI4c represents EM near-field distributions of such model along XY (Z= 0 nm) plane simulated at 45o of incident polarization. The interstitials marked as 1 and 4 located along diagonal axes (e.g. 45^{o} and 135^{o}) were found to possess the strongest EM near-field distributions of maximum intensity, E_{max}= 14.45 V/m. Figure 8d represents EM near-field distributions of the same model along XY (Z= 15 nm) plane simulated at 45^{o} of incident polarization. With reference to those observed in Fig. SI4b, the EM near-field distributions were found weak (E_{max}=4.01 V/m). Further insight for individual interstitials is demonstrated in insets (i)-(iv). Inset (i)-(ii) represent magnified view of the EM near-field distributions as marked by white dashed and black dashed squared in Fig. SI4a respectively. It was noted that the strongest EM near-field distribution (E_{max}= 14.11 V/m) was confined to interstitial 1 associated with a fairly strong EM near-field distribution at interstitial 2 (E_{max}=10.86 V/m) as shown in inset (i). The strongest EM near-field confinement at interstitial 1 was obvious because the incident polarization being parallel to the interparticle axis was favorable to the constructive dipole interaction at the interstitial marked by 1. Similarly, fairly strong EM near-field distributions were found confined at interstitial 4 and 5 (E_{max}= 14.28 and 11.08 V/m) along with a weak EM near-field distribution of Emax= 2.60 V/m at interstitial 3 as shown in inset (ii). It was noteworthy that the interstitials 2 and 5 were having reasonably high EM near-field distributions of E_{max}=10.86 and 11.08 V/m respectively, although these interstitials were out of in-plane axes in such scenarios. Inset (iii)-(iv) represent magnified view of the EM near-field distributions as marked by white dashed and black dashed squared in Fig. SI4b respectively. The strongest EM near-field distribution, E_{max}= 10.71 V/m was found confined at the junction of Au nanoparticles and Ag mist located near the interstitial 2, whereas the EM near-field distribution at

the junction of Au nanoparticle and Ag mist located near the interstitial 1 was found nearly half (E_{max}= 6.57 V/m) as shown in inset (iii). Inset (iv) represents the EM near-field distributions covering interstitials 3, 4, and 5. The strongest EM near-field confinement (E_{max}= 12.26 V/m) was observed at the junction of Au nanoparticle and Ag mist located near the interstitial 5 as shown in inset (iv). The junction of Au nanoparticle and Ag mist located near the interstitial 4 was having an EM near-field distribution of E_{max}= 3.87 V/m. With reference to those observed in inset (ii), the interstitials marked as 3 and 4 as shown in inset (iv) were found very weak with EM near-field distribution of E_{max}= 0.58 and 2.60 V/m respectively.

3.4 Revised Au tetramer model with additional five Ag mists:

It has been shown above in Fig. SI3-Fig. SI5 that there is a possibility to percolate and hybridize nearby localized energies depending on incident polarization. To the extent, such percolation and hybridization occur on different planes as well provided that the topographic twists happened in nanometric scale in corresponding planes. For example, the EM near-field distributions at planes XY (Z= 0 nm), and XY (Z= 15 nm) for pristine tetramer and decorated tetramer have been demonstrated in Fig. SI3-Fig. SI5 for s-, p- and 45^{o} of incident polarizations. Zoom-in views therein predicted possibilities of nearby confined energies at such two planes. This is noteworthy that the possibility of such percolation relies on the variation of topographic structures in nanoscale. Therefore the more the topography changes in different planes, the more the possibility rises for percolation and hybridization of nearby confined energies.

To understand the percolation of confined energy, the same Au tetramer model was revised further placing additional five Ag nanoparticles at XY (Z= 12 nm) plane. The Ag nanoparticles were amended in such a way so that the additional nanoparticles are positioned at the available five

interstitials of the same tetramer. For the convenience of comparison, the revised model was simulated for excitation of 647 nm at s-, p- and 45° of incident polarizations. EM near-field distributions of the revised model were extracted for XY (Z= 0 nm), XY (Z= 12 nm) and XY (Z= 15 nm) planes as shown in Fig. SI6.

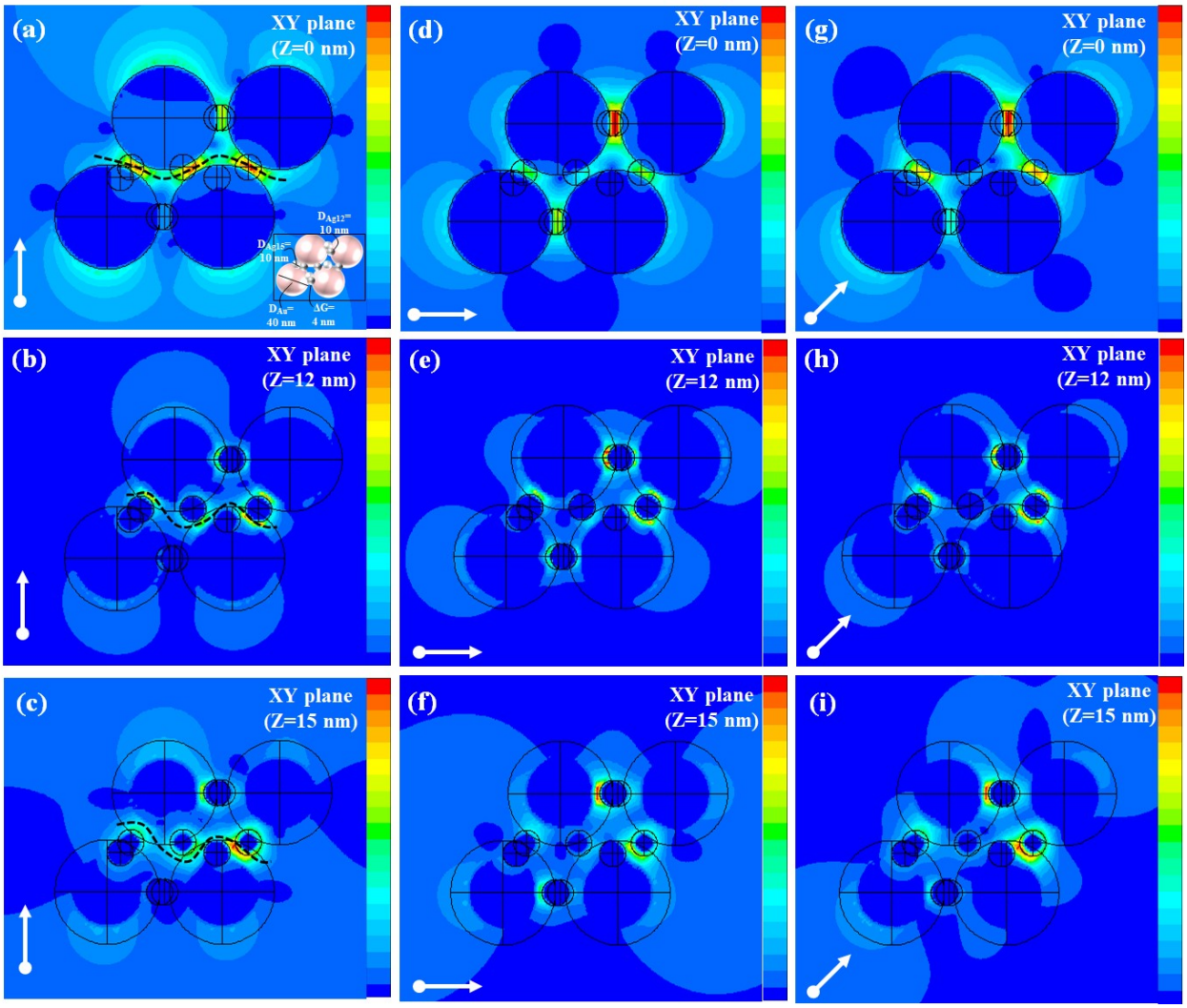

Figure SI6. (a)-(b) EM near-field distributions at three different planes (XY (Z= 0 nm), XY (Z= 12 nm) and XY (Z= 15 nm)) respectively of the same model as shown in the inset of Fig. SI6a and simulated for excitation of 647 nm at p-polarization; the black dashed lines represent plausible percolation of nearby localized energies, (d)-(f) The same distributions of the same model for three different planes respectively and simulated at s-polarization and (g)-(i) The same distributions of the same model for three different planes respectively and simulated at 45° of incident polarizations. White arrows in each figure represent polarization directions of incident excitation. Colour bars represent the respective intensities observed under the simulations.

4. Estimation of SERS enhancement factor:

To understand or quantify the number of dyes adsorbed on the SERS-active substrate is crucial to determine the enhancement factor. The group has elaborated the estimation of the dyes in this regard elsewhere (Phys. Chem. Chem. Phys., 2012, 14, 10132-10139). However, in this current study, the enhancement factors were obtained following the revised formula,

$$EF = \left(\frac{I_{SERS}}{I_{bulk}}\right) \times \left(\frac{N_{bulk}}{N_{SERS}}\right),$$

whereas the ratio between N_{bulk} and N_{SERS} is equal to the ratio between C_{bulk} and C_{SERS} (i.e. $\frac{N_{bulk}}{N_{SERS}} = \frac{C_{bulk}}{C_{SERS}}$). The detailed calculation can be shown as follows.

As per the abovementioned reference, the number of analytes in bulk condition was calculated according to the following formula

$$N_{bulk} = \frac{C_{bulk} \times V_{bulk} \times N_A}{A_{drop} \times D_{laser}} \qquad \text{(eq. 1)}$$

where N_{bulk}, C_{bulk}, V_{bulk}, N_A, A_{drop} and D_{laser} represent the number of analytes, concentration of dye, volume of dye solution, Avogadro number, area of the droplet in incubation and laser spot diameter in Raman measurements respectively.

The number of analytes in the SERS condition was calculated according to the following formula

$$N_{SERS} = \frac{C_{SERS} \times V_{SERS} \times N_A}{A_{drop} \times D_{laser}} \qquad \text{(eq. 2)}$$

where N_{SERS}, C_{SERS}, V_{SERS}, N_A, A_{drop} and D_{laser} represent the number of analytes, concentration of dye, volume of dye solution, Avogadro number, area of the droplet in incubation and laser spot diameter in SERS measurements respectively.

In this current study, the volume of dye solution and laser spot diameter remained the same in all the Raman and SERS measurements. The areas of the droplet in incubation in both cases will be the same because of the same volume of dye solution. Therefore, solving the eq. 1 and eq. 2, one can notice, the ratio between the number of dyes adsorbed on nanoassemblies (i.e. PGNA or MGNA) and that at bulk condition is,

$$\frac{N_{bulk}}{N_{SERS}} = \frac{C_{bulk}}{C_{SERS}}$$